**Energy Materials**

Article

# Accelerating redox kinetics by ZIF-67 derived amorphous cobalt phosphide electrocatalyst for high-performance lithium-sulfur batteries

**Junan Feng[1], Jiayi Li[1], Hongwei Zhang[1], Wendong Liu[1], Zenghui Lin[1], Tianyi Wang[3], Bing Sun[4], Xiaoxian Zhao[2,*], Fengyun Wang[1,*], Jianjun Song[1,*]**

[1]College of Physics, Qingdao University, Qingdao 266071, Shandong, China.
[2]Department of Chemistry, College of Science, Hebei Agricultural University, Baoding 071001, Hebei, China.
[3]School of Chemistry and Chemical Engineering, Yangzhou University, Yangzhou 225002, Jiangsu, China.
[4]Centre for Clean Energy Technology, School of Mathematical and Physical Sciences, Faculty of Science, University of Technology Sydney, Sydney, NSW 2007, Australia.

*\***Correspondence to:** Prof. Xiaoxian Zhao, Department of Chemistry, College of Science, Hebei Agricultural University, No. 289, Lingyusi Street, Baoding 071001, Hebei, China. E-mail: lxzhxx@hebau.edu.cn; Prof. Fengyun Wang, College of Physics, Qingdao University, No. 308, Ningxia Road, Shinan District, Qingdao 266071, Shandong, China. E-mail: fywang@qdu.edu.cn; Prof. Jianjun Song, College of Physics, Qingdao University, No. 308, Ningxia Road, Shinan District, Qingdao 266071, Shandong, China. E-mail: jianjun.song@qdu.edu.cn

## Abstract

The feasibility of the commercialization of lithium-sulfur (Li-S) batteries is troubled by sluggish redox conversion kinetics and the shuttle effect of polysulfides. Herein, a zeolitic imidazolate framework derived amorphous CoP combined with carbon nanotubes conductive network composites (aCoP@CNTs) has been synthesized as an effective dual-electrocatalyst for accelerating the redox kinetics of polysulfides to prolong the lifespan of Li-S batteries. Compared with crystalline CoP, unsaturated Co atoms of aCoP@CNTs exhibit stronger chemical adsorption capacity for polysulfides and serve as catalytic centers to accelerate the conversion from soluble polysulfides to solid-state lithium sulfide. Meanwhile, the 3D porous conductive network not only facilitates ion/electron transportation but also forms a physical barrier to limit the migration of polysulfides. Benefiting from the above preponderances, the batteries with aCoP@CNTs modified interlayer exhibited excellent cycle stability (initial discharge capacity of 1227.9 mAh g$^{-1}$ at 0.2 C), rate performance (795.9 mAh g$^{-1}$ at 2.5 C), long-term cycle reliability (decay rate of 0.049% per cycle at 1 C over 1000 cycles), and superior high-loading performance (high

initial discharge capacity of 886 mAh g$^{-1}$ and 753.6 mAh g$^{-1}$ at 1 C under high S loading of 3 mg cm$^{-2}$ and 4 mg cm$^{-2}$).

## INTRODUCTION

For the last few years, lithium-sulfur (Li-S) batteries have attracted widespread attention owing to their natural advantages of the high theoretical energy density of 2600 Wh kg$^{-1}$ and theoretical specific capacity of 1675 mAh g$^{-1}$, abundant raw material reserves, and environmentally friendly[1-3]. Nevertheless, the practical development of Li-S batteries still faces several fatal obstacles: (i) the insulator nature of sulfur and its discharge product Li$_2$S$_2$/Li$_2$S leads to low utilization of active materials; (ii) soluble polysulfides (PSs) intermediates dissolved in the electrolyte and shuttled back and forth between the cathode and anode sides (the shuttle effect), which leads to the reduction of coulomb efficiency and the rapid decline of capacity; and (iii) the drastic volume change of sulfur cathode during cycling[4-6].

Considerable efforts have been made to conquer the above technical challenges, including designing sulfur host of rational structures with various functional materials[7-10], modifying separator functionalization[11-14], and optimizing electrolytes[15-17]. Among them, separator functionalization exhibits unique advantages due to its traits of facile preparation and direct PSs intercept; meanwhile, the multifunctional coating of separator severs as upper current collectors extend the path for ions migration and ensure fast ion transmission[18]. Up to now, a variety of functional materials have been introduced to modify separators for the enhancement of the electrochemical performance of Li-S batteries. The nanoscale nonpolar carbon material, such as porous carbon spheres, carbon nanotubes (CNTs)[19,20], carbon nanofiber (CNF)[21], graphene oxide (GO)[22] and metal-organic frameworks (MOFs) derived carbon[23,24], were widely studied as the functional coating to ease the shuttle effect of PSs due to high conductively and specific surface area via physical adsorption[25]. For example, Manthiram's group applied multi-walled CNT to spread on one side of the conventional polypropylene (PP) separator by using a facile vacuum filtration method, the high specific surface area brought by MWCNT provides many adsorption sites for PSs; thus, the Li-S batteries with the modified separator retain 621 mAh g$^{-1}$ after 300 cycles[26]. Zhou *et al.* prepared a GO-coated separator and used it in Li-S battery under a high sulfur loading of 4 mg cm$^{-2}$, and the cells achieved a high initial capacity of 1006 mAh g$^{-1}$ at 0.9 C with an attenuation rate of 0.1% per cycle after 300 cycles[27].

Unfortunately, the practical application of Li-S batteries demands high content of sulfur load into the cathode, and thus the nonpolar carbon material, which only possesses weak chemical interaction between PSs and the poor ability of electrocatalysis, cannot further inhibit the dissolution of PSs and enhance redox kinetics during discharge/charge process, resulting in disappointing long-term cycle stability[28,29]. Therefore, polar materials, which both possess the dual-function of robust chemical adsorption between sulfur species and enhancement of electrocatalysis kinetics for the redox process, have attracted extensive attention. For instance, metal oxides (Fe$_3$O$_4$, MnO$_2$, Co$_3$O$_4$)[30-33], transition metal phosphide (FeP, CoP)[34,35], metal carbides (Fe$_3$C, Ti$_3$C$_2$)[36,37], and metal selenide (ZnSe, FeSe$_2$)[38,39] combined with a series of unique designed carbon construction have been deeply investigated. In particular, some specific amorphous metal compounds have been demonstrated to possess stronger catalytic ability than their crystalline state. Recent research has revealed that the unsaturated electronic configuration of amorphous metal compounds may improve the electronic conductivity, and the rich defect sites and dangling bonds could strengthen the chemical interaction with PSs, therefore effectively inhibiting the shuttle effect[40]. For example, Li *et al.* successfully prepared amorphous cobalt oxide nanosheets as cathode additives for Li-S battery, and the DFT calculations suggested the *d* orbital redistribution of amorphization CoO could further strengthen chemical bonding

energy of PSs, and thus exhibited satisfactory rate performance and cycle stability[41]. Therefore, the amorphous metal compounds possess great potential in enhancing the chemical polar adsorption and redox rate of PSs in Li-S kinetics.

Herein, we report a ZIF-67 derived amorphous CoP combined with carbon nanotubes conductive network composites (aCoP@CNTs) as a functional electrocatalytic interlayer to restrict the shuttle effect and enhance the redox kinetics in Li-S battery. The embedded 3D network can not only effectively promote the transmission of electrons and reduce the impedance of the interface, but also serve as an ion-sieving layer and physical barrier to prevent the diffusion of PSs. In addition, the amorphous CoP uniformly dispersed on the carbon matrix could further fix PSs on the cathode side via robust Co-S chemical bonding interaction[42,43]. More importantly, results demonstrated that the amorphous CoP contributes to superior electrocatalysis kinetics redox for sulfur confinement compared with crystalline CoP. Therefore, benefitting from the synergistic effect of physical/chemical adsorption toward PSs and electrocatalysis function, the Li-S battery with electrocatalytic aCoP@CNTs separator demonstrates robust electrochemical performance with a good initial discharge capacity of 1014.4 mAh g$^{-1}$ at 1 C, and excellent long-term cycle stability at high S loading at 1 C.

## EXPERIMENTAL

### Synthesis of ZIF-67@CNTs composites

50 mg Polyvinylpyrrolidone (PVP) and 30 mg CNTs treated with nitric acid were dispersed ultrasonically in 20 mL methanol for 1 h to form a uniform suspension. $CoH_{12}N_2O_{12}$ (0.582 g, Aladdin, AR, 99%) was added to the above suspension and stirred for 1 h. Then 10 mL methanol containing 0.648 g of 2-methylimidazole (Aladdin, AR, 99%) was quickly poured into the above suspension. The solution was stirred for 20 min and aged 24 h. Finally, the ZIF-67@CNTs composites were collected via centrifugation, washed with ethanol four times, and vacuum-dried at 80 °C for a night.

### Synthesis of aCoP@CNTs and cCoP@CNTs composites

aCoP@CNTs sample was obtained by an *in-situ* phosphating method. Briefly, the as-synthesized ZIF-67@CNTs and $NaH_2PO_2$ were placed on the downstream and upstream side of the tubular furnace with a mass ratio of 1:4, respectively, and further calcined in an argon atmosphere at 350 °C for 2 h. The synthesis of cCoP@CNTs was the same as the above route except that the ZIF-67@CNTs were further annealed in a nitrogen atmosphere at 700 °C for 2 h to form CoO@CNTs before phosphating.

### Synthesis of aCoP@CNTs, cCoP@CNTs and KB modified separators

To fabricate the aCoP@CNTs/cCoP@CNTs modified separators, 50 wt% of the aCoP@CNTs/C composite was mixed with 40 wt% of Ketjen Black (KB) and 10 wt% of polyvinylidene difluoride (PVDF) in N-Methylpyrrolidone (NMP) and ground uniformly to form a slurry, then, the slurry was coated on one side of PP separator (Celgard 2400). As a contrast sample, KB and PVDF were mixed with a mass ratio of 9:1 and coated on PP separator according to the above same process. After being dried at 60 °C for one night, the modified separators were punched into circular pieces of φ19 mm. The average loading of functional material on each separator is 0.16 mg cm$^{-2}$.

### Preparation of the KB/S cathode

The KB/S cathode was prepared via a traditional melt-diffusion method. A uniform mixture of sublimed sulfur and KB with a mass ratio of 7:3 was put into an autoclave and maintained at 155 °C for 12 h to obtain KB/S composites. The KB/S cathode was uniformly mixed with KB and PVDF in NMP and smooth coated on the aluminum foil. Finally, dried in vacuum at 60 °C for 10 h. The high-load sulfur electrode is prepared with the same KB/S composite material as above, and the cathodes under different S loading are obtained by

adjusting the thickness of the scraper.

## Preparation of $Li_2S_6$ and $Li_2S_8$ solution

$Li_2S_6$ electrolyte was synthesized by reacting lithium sulfide and sulfur powders in 1,3-dioxolane (DOL) and 1,2-dimethoxyethane (DME) (VDOL:VDME = 1:1) with a moral mass ratio of 5:1 under vigorous stirring for 48 h in the glovebox.

$Li_2S_8$ electrolyte was synthesized by magnetically stirring lithium sulfide and sulfur powders with a moral mass ratio of 7:1 in tetraglyme for 48 h in the glovebox.

## Catalytic performance tests

aCoP@CNTs, cCoP@CNTs, and KB were mixed with PVDF in NMP to form a uniform slurry with a mass ratio of 4:1, then the slurry was coated on carbon-coated aluminum foil and dried under vacuum at 60 °C for 12 h. the electrodes without sulfur loading were cut into circular pieces of φ12 mm.

$Li_2S_6$-symmetric cells CV test: The symmetric cells were fabricated with the above identical electrode under an Ar atmosphere using 0.2 M $Li_2S_6$ electrolyte in the glovebox. The CV measurements voltage range was from -1.4 to 1.4 V with a scan rate of 0.01V $s^{-1}$.

Nucleation and dissolution of $Li_2S$ test: The asymmetrical cells were assembled by the above electrode as a cathode, lithium foil as an anode, 20 μL $Li_2S_8$ electrolyte as catholyte, and 20 μL 1.0 M LiTFSI and 2.0 wt% $LiNO_3$ dissolved in DME and DOL ($V_{DOL}:V_{DME}$ = 1:1) solution as anolyte. For the nucleation test, the batteries were first galvanostatic discharged to 2.06 V with a current value of 0.112 mA, and then were potentiostatic discharged until the current value was close to 0.01 mA at 2.05 V. For the dissolution test, the batteries were first galvanostatic discharged to 1.8 V at 0.1 mA, and then were further potentiostatic discharged to 1.8 V at 0.01 mA to ensure $Li_2S$ is fully formed, finally, the batteries were potentiostatic charged until the current value is close to 0.01 mA at 2.4 V.

## Cells assembly and electrochemical testing

Typically, Li-S coin cells (CR2032) were assembled with lithium foil as an anode, KB/S compound as cathode, and 1.0 M LiTFSI and 1.0 wt% $LiNO_3$ dissolved in DME and DOL ($V_{DOL}:V_{DME}$ = 1:1) as the electrolyte in $O_2$ and $H_2O$ < 0.1 ppm circumstances. The diameter and the sulfur loading of the KB/S cathode are 12 mm and 0.8~1 mg $cm^{-2}$. The amount of electrolyte is ~15 μL. The performance of Li-S battery at high sulfur loading of 3.1 and 4.06 mg $cm^{-2}$ with electrolyte/ sulfur (E/S) ratio of ~5.0 μL $mg^{-1}$ was also evaluated. The modified layer of the separator faces the cathode side. The different scan rates of cyclic voltammetry (CV, voltage windows of 1.7-2.8 V) and electrochemical impedance spectroscopy (EIS, frequency range from 0.01 Hz to 100 kHz, AC voltage amplitude of 5 mV.) dates were gauged on a CHI760E electrochemical workstation. The galvanostatic charge/discharge and cycle performance dates were collected on Land CT2001A battery test system with a voltage range of 1.7-2.8 V.

## Materials characterization

The phase information of materials was analyzed by XRD (Cu Ka radiation with k = 1.5405 Å) in the angle range of 5° to 80°. The structure and morphologies of the materials were analyzed by SEM (Nova Nano SEM450, 15k eV) and TEM (JEOL JEM 2100F). The specific surface area and pore size of the samples were measured by $N_2$ adsorption/desorption isotherms (77 K, Tristar 3000). XPS was performed on ESCALAB 250 to study the chemical valence state of the samples. The elemental distribution of the materials was analyzed by HRTEM and attached EDS equipment (Oxford Instruments and EDAX).

## RESULTS AND DISCUSSION

The ZIF-67@CNTs precursor was prepared by a modified precipitation method. As shown in Figure 1A, ZIF-67@CNTs precursor was first synthesized through the reaction of 2-methylimidazole in methanol and the mix suspension of $Co^+$ and CNTs, and then the aCoP@CNTs was obtained through directly phosphating ZIF-67@CNTs precursor. While the cCoP@CNTs were synthesized via annealing to perform CoO@CNTs and then converted to cCoP@CNTs via phosphorization. SEM and TEM were used to deeply investigate the microstructure of obtained electrocatalyst. Supplementary Figure 1 shows morphologies of obtained ZIF-67@CNTs precursor, the CNT was well-fdistributed grown on the typical ZIF-67 crystal smooth polyhedron. After phosphating at 350 °C, no obvious change in the morphology [Figure 1B, Supplementary Figure 2], aCoP@CNTs maintains the classic structure of polyhedron, the amorphous CoP was attached to the ZIF-67 derived carbon skeleton with the size of 300~400 nm; meanwhile, the uniform distribution of CNTs would effectively ensure the conductivity of the electrocatalyst. SEM image of cCoP@CNTs in Figure 1C exhibits the similar construction to aCoP@CNTs. Further, the TEM image [Figure 1D] of the aCoP@CNTs suggests that the CNTs with a diameter of ~10 nm are closely combined with the interface of amorphous CoP and formed a highly conductive network. More significantly, no obvious lattice fringe appears in the lattice-resolved high-resolution TEM images of aCoP@CNTs [Figure 1F], further proving the successful preparation of amorphous CoP[44]. cCoP@CNTs maintains a similar structure to aCoP@CNTs [Figure 1E], while the crystalline properties of CoP are affirmed by its clear lattice stripes [Figure 1G]. The obvious lattice fringes of 0.282 nm and 0.189 nm correspond to the (202) and (111) crystalline planes of orthorhombic phased CoP[45]. The energy dispersive spectroscopy (EDS) mapping analysis for the two electrocatalysts shown in Figure 1H and I indicated the homogeneous distribution of Co, N, O, P, and C elements.

The XRD patterns of pure ZIF-67 and ZIF-67@CNTs in Supplementary Figure 3 show similar characteristic peaks of ZIF-67. Figure 2A shows XRD patterns of aCoP@CNTs and cCoP@CNTs samples after phosphidation. The intense diffraction peaks of the two samples at ~26° correspond to the characteristic peak of carbon. The characteristic peaks of cCoP@CNTs are well indexed to orthorhombic CoP (PDF#29-0497), consistent with the characterization results of HRTEM. In contrast, no obvious diffraction characteristic peak is found for aCoP@CNTs, further demonstrating its amorphous trait[46]. X-ray photoelectron spectroscopy (XPS) is used to analyze the valence and structure of compounds. The full XPS spectrum of aCoP@CNTs and cCoP@CNTs in Figure 2B and Supplementary Figure 4 suggest the existence of Co, P, N, C, and O elements, and the result matches well with the EDS elemental mapping. The high-resolution XPS spectrum of Co 2p for aCoP@CNTs and cCoP@CNTs is shown in Figure 2C. For aCoP@CNTs, the Co 2p spectrum primarily consists of Co $2p_{3/2}$ and Co $2p_{1/2}$ peaks. The Co $2p_{3/2}$ spectrum could be further fitted and divided into three peaks, which were assigned to Co-O (782.4 eV), Co-P (779.1 eV) and satellite signal (786.32 eV). The peaks at 798.4 and 804.26 eV correspond to Co-O and satellite peaks in Co $2p_{1/2}$[42]. Similarly, the Co $2p_{3/2}$ HRXPS of cCoP@CNTs dispatched into three peaks at 779.3, 782.8, and 786.4eV corresponding to Co-P, Co-O, and the satellite signal, respectively[47]. The peak deconvolution of the P 2p for aCoP@CNTs in Figure 2D exhibit obvious peaks at a binding energy of 134.3 and 135.2 eV, which suggests the existence of oxidized phosphorus species in CoP. The peak at a binding energy of 130.2 eV corresponds to the bond of Co-P[48]. The spectra of graphitic-N, pyrrolic-N, and Co-N of aCoP@CNTs are marked at a binding energy of 399.6, 400.3, and 401.1 eV in Figure 2E, respectively[49]. Figure 2F shows the C 1s spectrum of aCoP@CNTs with two fitted characteristic peaks at 284.7 and 285.3 eV, which corresponds to the C=C and C-C in CNTs[50]. In addition, the P 2p HR-XPS spectrum of cCoP@CNTs is shown in Supplementary Figure 5, the characteristic peak of Co-P is located at 130 eV, and the peaks at 134.8 and 136.1 eV correspond to P-O bonding in cCoP@CNTs[51]. More significantly, compared with cCoP@CNTs, the binding energy (BE) of the Co-P characteristic peak in Co $2p_{3/2}$ shifts to a
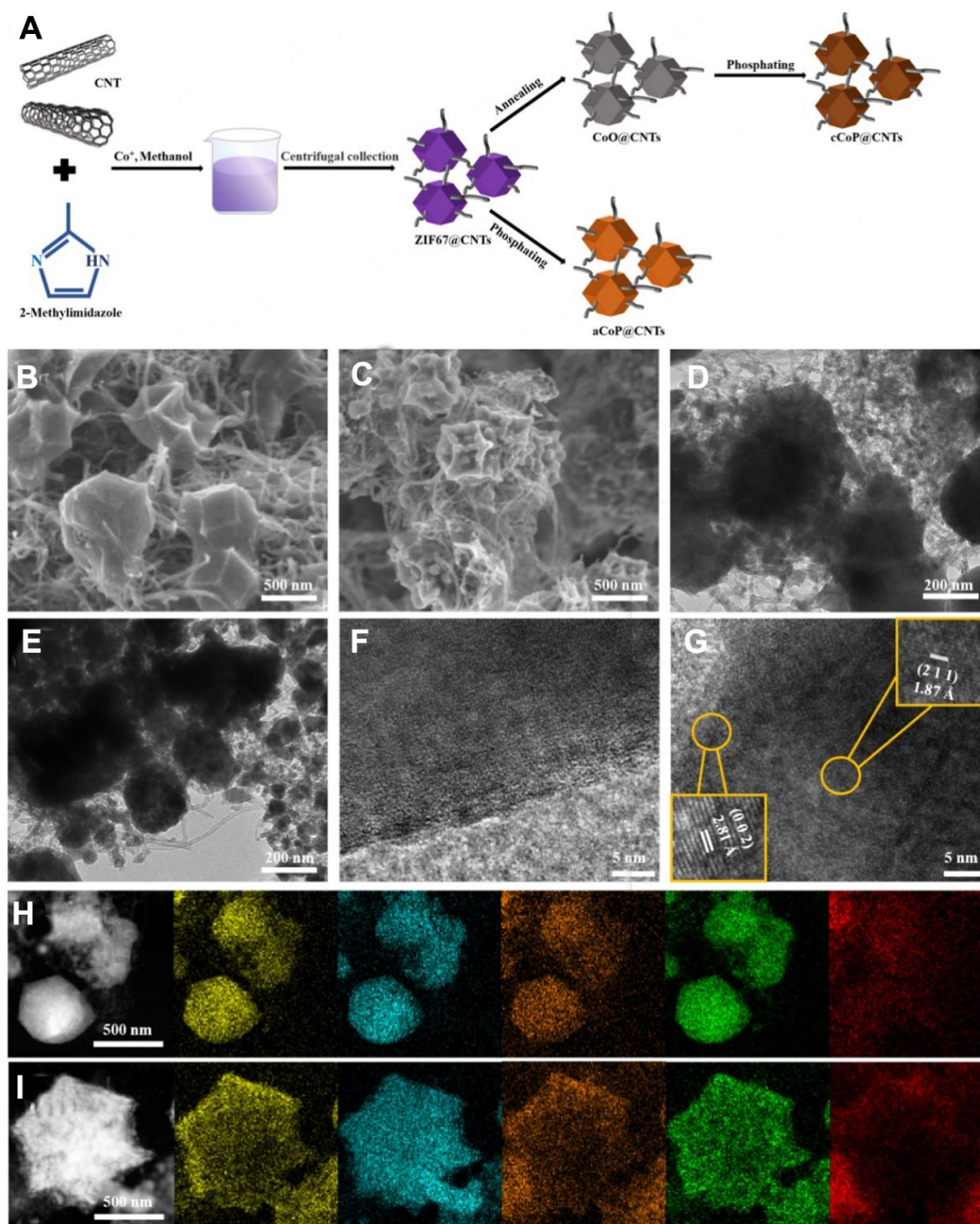
**Figure 1.** (A) Diagrammatic sketch of synthesis route of aCoP@CNTs and cCoP@CNTs; SEM images of (B) aCoP@CNTs and (C) cCoP@CNTs; TEM images of (D) aCoP@CNTs and (E) cCoP@CNTs; HRTEM images of (F) aCoP@CNTs and (G) cCoP@CNTs; HAADF-STEM image and EDX mappings of (H) aCoP@CNTs and (I) cCoP@CNTs.

lower BE position, while the Co-P characteristic peak shifts to higher BE in P 2p spectrum, indicating the presence of ample unsaturated bonds in aCoP@CNTs. Due to the fracture of atom long-range ordered, amorphous materials possess a feature of short-range order structure, which may contribute to a unique surface electronic state, further enhancing the chemical adsorption of PSs[52].
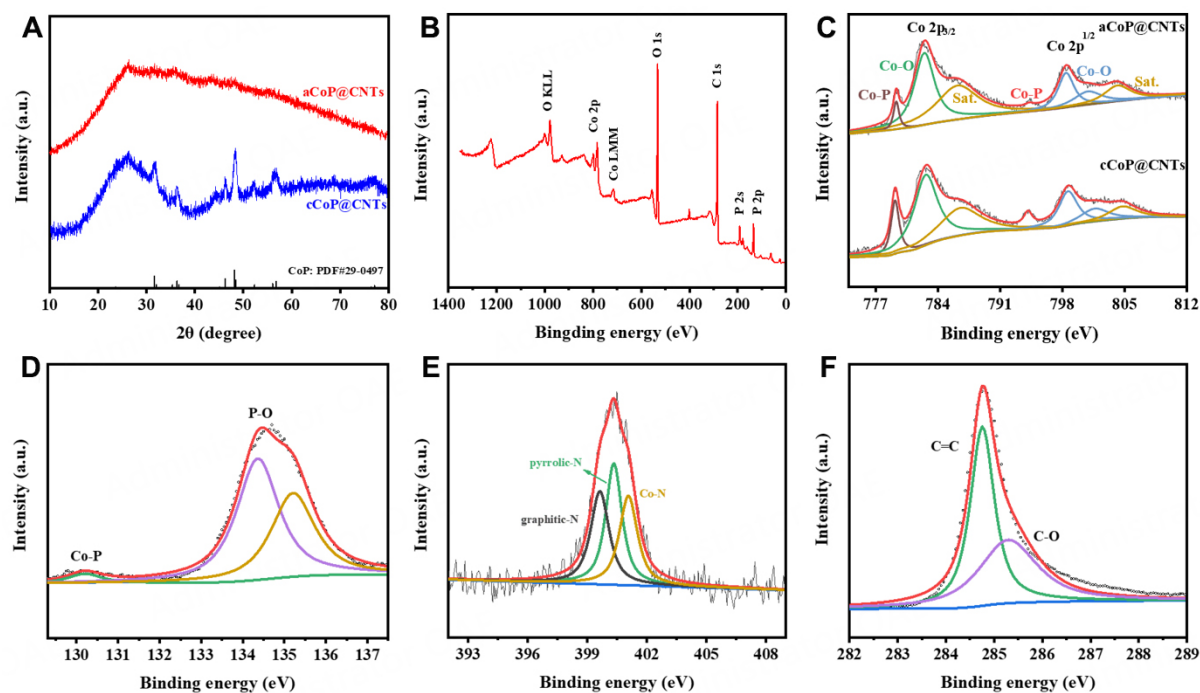
**Figure 2.** (A) XRD patterns of aCoP@CNTs and cCoP@CNTs; (B) full-scan XPS spectra of aCoP@CNTs; (C) Co 2p HRXPS spectra of aCoP@CNTs and cCoP@CNTs, HRXPS spectra of aCoP@CNTs: (D) P 2p; (E) N 1s; (F) C 1s.

To further verify the superiority of aCoP@CNTs modified separator in ion migration behavior, the impedance of stainless steel (SS)|modified separator|SS batteries at different temperatures were tested and obtained the corresponding ionic conductivity, as shown in Supplementary Figure 6 and Figure 3A. Specifically, the aCoP@CNTs exhibit the highest ionic conductivity of 0.999, 1.052 and 1.129 cm$^{-1}$ at 30, 40 and 50 °C. Besides, the activation energy corresponding to the above battery is calculated by Arrhenius equation [Figure 3B][53]. The calculated activation energies of aCoP@CNTs, cCoP@CNTs, KB, and PP are 0.0316, 0.0392, 0.0534, and 0.0911 eV, respectively, which suggest that the introduction of amorphous CoP active sites on interconnect CNTs effectively improves the mobility of ions, benefiting the fast Li$^+$ transmission.

The Li$_2$S$_6$-symmetric cells were assembled to evaluate the catalytic potentiality of amorphous CoP particles for soluble PSs intermediates. Specifically, the interlayer materials serve as the identical working electrode and counter electrode, and 10 μL 1M Li$_2$S$_6$ solution act as electrolyte. CV profiles were acquired over the voltage range from -1.4 V to 1.4 V at a scan rate of 10 mV s$^{-1}$. Figure 3C shows that the aCoP@CNTs symmetric cells exhibit the highest current density and the smallest voltage difference between symmetrical oxidation peaks and reduction peaks, implying the increase of catalytic activity for PSs conversion compared to the cCoP@CNTs electrode. The potentiostatic discharge testing of Li$_2$S$_8$ electrolytes on different interlayer materials further proves the superiority of the aCoP@CNTs in catalyzing Li$_2$S nucleation and growth. Specifically, the aCoP@CNTs [Figure 3D] possess the highest current density, and shortest nucleation time of Li$_2$S compared with cCoP@CNTs [Figure 3E] and KB [Figure 3F], the Li$_2$S nucleation capacity of aCoP@CNTs (171.7 mAh g$^{-1}$) was also much higher than that of cCoP@CNTs (130.7 mAh g$^{-1}$) and KB (63.3 mAh g$^{-1}$). Relatively, the dissolution of the Li$_2$S test further confirmed the efficient selective catalysis of the amorphous CoP[54]. As shown in Supplementary Figure 7, contrasted with cCoP@CNTs and KB, aCoP@CNTs achieved a shorter dissolution time (2871 s) and a higher current peak, thus delivering a high dissolution capacity of Li$_2$S (420.4 mAh g$^{-1}$).
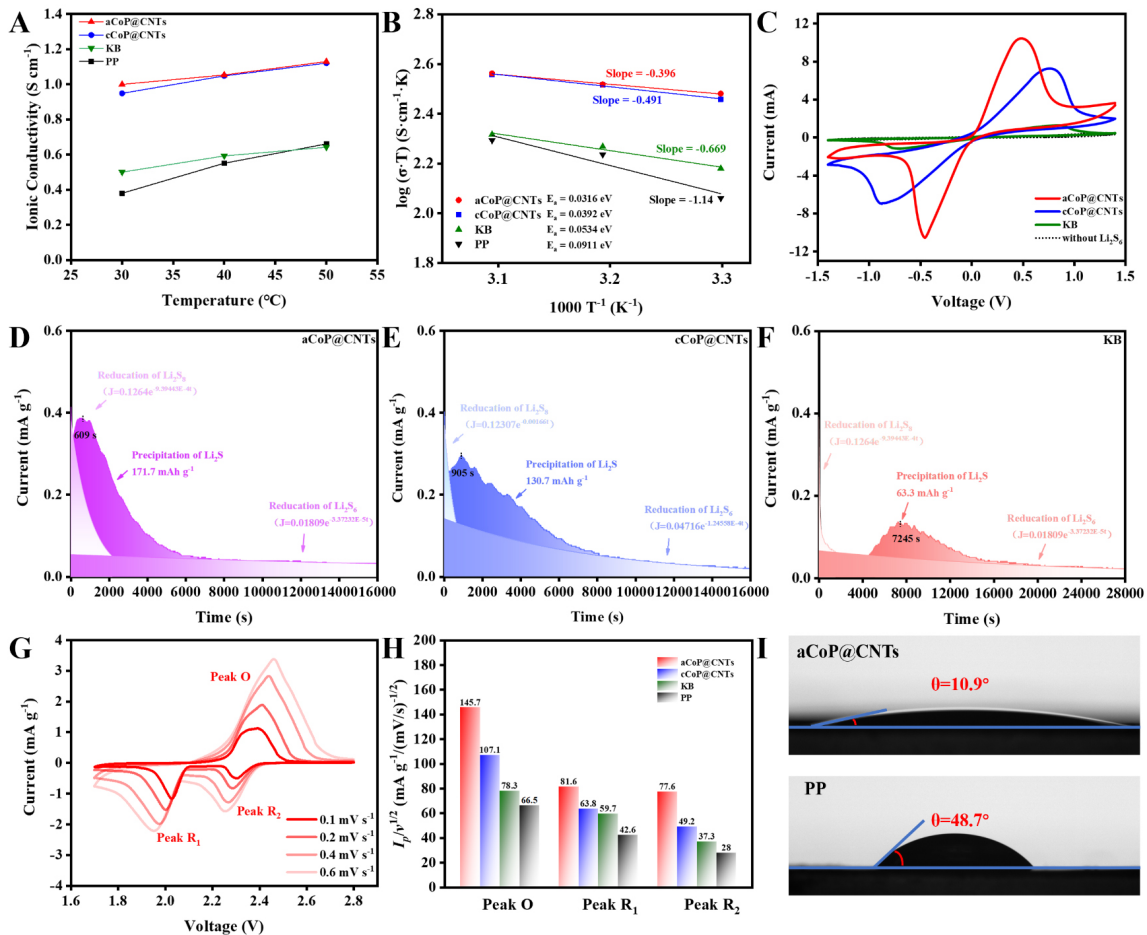
**Figure 3.** (A) Ion conductivity of different modified separators; (B) activation energy of different materials derived from ionic conductivity; (C) CV curves of the $Li_2S_6$-symmetric cells with as-fabricated functional interlayer materials; the fitting curves of $Li_2S$ deposition on the surface of aCoP@CNTs (D), aCoP@CNTs (E) and KB (F); (G) CV curves with different scan rates of the Li-S batteries with aCoP@CNTs; (H) slope value of fitting linear curves of the peak currents versus square roots of scan rate; (I) contact angle of aCoP@CNTs and PP separators.

The $Li^+$ ion diffusion behaviors of different materials were evaluated by deriving from the CV curves at scanning rates of 0.1 mV s$^{-1}$ to 0.6 mV s$^{-1}$. The intensity of redox peaks gradually becomes stronger with the increase in scan rates, and the potential difference between cathode peaks and anode peak decrease by degrees [Figure 3G, Supplementary Figures 8 and 9]. The fitting results of three peaks via Randles-Sevcik Equation: (1) $I_p = 2.65 \times 10^5 n^{3/2} a D_{Li}^{+1/2} v^{1/2} C_{Li}^+$ and shown in Figure 3H[55,56]. The slope of aCoP@CNTs was higher than aCoP@CNTs and KB in different peaks, confirming the better diffusion kinetics of aCoP@CNTs[57]. Galvanostatic cycling performance of Li symmetric batteries with aCoP@CNTs and PP was assembled to evaluate the interfacial stability and plating/stripping effect of the aCoP@CNTs on regulating the Li deposition of the anode. As shown in Supplementary Figure 10, the polarization for the cCoP@CNTs separator exhibit a sharp increase after the continuous Li plating/stripping process after 170 h owing to the growth of Li dendrites and serious side effects. Contrarily, the aCoP@CNTs separator maintained a flat plateau with a low overpotential of 25.9 mV even after 300 h, which proves a positive effect of the aCoP@CNTs on the regulation of Li deposition[58].

The wettability of aCoP@CNTs and PP separators to the electrolyte was characterized by a contact angle test. As exhibited in Figure 3I, after dropping the same volume of electrolyte on the surface of the separator, a large contact angle of 48.7° is observed on the surface of PP. Impressively, the contact angle of aCoP@CNTs decreased to 10.9°, much smaller than that of PP separator, indicating that the electrolyte can rapidly infiltrate the aCoP@CNTs coating.

The cross-sectional image [Figure 4A] shows that the coating thickness of aCoP@CNTs modified interlayer is only about 8.4 μm and the average functional materials loading amount of only 0.17 mg cm$^{-2}$ in each separator. The electrochemical performance corresponding to the above analysis of catalytic capacity was also characterized. Figure 4B shows the CV curves of the Li-S cells with three kinds of separators. All cells exhibit typical one anode peak and two cathode peaks, and the two reduction peaks located at ~2.30 V and ~2.06 V correspond to two reduction steps of $S_8$ to $Li_2S_x$ (8 ≥ x ≥ 4) and $Li_2S_4$ to $Li_2S_2/Li_2S$, respectively. The oxidation peak at ~2.40 V represents the conversion to elemental sulfur. In addition, the batteries with aCoP@CNTs show stronger and shaper current corresponding peaks than other cells, further indicating better redox reaction kinetics of PSs. Meanwhile, as shown in Supplementary Figure 11, the well-overlapped CV curves, except for the first cycle of aCoP@CNTs, proved good cycling reversibility. The cycle performance at 0.2 C in Figure 4C shows that the batteries with aCoP@CNTs modified separator delivered the highest initial discharge specific capacity of 1227.9 mAh g$^{-1}$. After 200 cycles, the batteries remain a high reversible capacity of 814 mAh g$^{-1}$, much higher than that of cCoP@CNTs and KB separators (665.5 and 357.3 mAh g$^{-1}$, respectively). The first charge/discharge profiles of all cells at 0.2 C in Figure 4D exhibit two typical discharge plateaus, corresponding to the CV analysis. The initial potentials of the first charge profile were obtained in Figure 4E and could be regarded as the activation energy barrier of $Li_2S$. The lowest potential (1.87 V) of aCoP@CNTs means the fast conversion of $Li_2S$ to PSs, demonstrating the outstanding electrocatalytic performance of amorphous CoP. Meanwhile, as shown in Figure 4D, the aCoP@CNTs batteries show the minimum value (142 mV) of a voltage difference (ΔE) compared to cCoP@CNTs (160 mV), KB (165 mV), and PP (279 mV), indicating that amorphous CoP can promote the chemical adsorption and effective conversion for PSs. It is worth noting that the second discharge plateau contributes 75% of the theoretical specific capacity in Li-S batteries, and thus the ratio of specific capacity origins from a low plateau and high plateau ($Q_L/Q_H$) was also calculated in Figure 4F. Compared with KB and PP modified separators, the batteries with aCoP@CNTs or cCoP@CNTs delivered a higher value of $Q_L/Q_H$, indicating the full utilization of sulfur species in the process for PSs to $Li_2S_2/Li_2S$.

Beneficial from the synergistic effect of chemical limitations and excellent electrocatalyst capacity for PSs, the batteries with aCoP@CNTs also delivered satisfying rate performance with 1513.5, 1223.4, 1063.8, 965.5, 903.5, 848.8, 795.9 mAh g$^{-1}$ at 0.1, 0.2, 0.5,1, 1.5, 2 and 2.5 C, respectively [Figure 4G]. Profiting from the robust chemical interaction with PSs and amorphous CoP, the shuttle effect has been greatly alleviated. When the current density was back to 0.2 C, the batteries still maintained a high reversible capacity of 1130.3 mAh g$^{-1}$. However, the batteries with cCoP@CNTs, KB, and PP only remained 691.9, 498.1, 280.3 mAh g$^{-1}$ at a high rate of 2.5 C, respectively. Moreover, the charge/discharge plateaus of aCoP@CNTs extracted from the rate performance were also investigated in Supplementary Figure 12; the overpotential increases gradually with the increment of current density; however, even when the current density increase to 2.5 C, the two typical discharge plateaus could be observed obviously, indicating that the introduction of amorphous CoP electrocatalyst was a reasonable way to improve the electrochemical performance of Li-S battery. As shown in Figure 4H, the long-term cycling stability of different batteries at 1 C shows that the aCoP@CNTs cells possess a high initial capacity of 1014.4 mAh g$^{-1}$ and retain a satisfying reversible capacity of 521.9 mAh g$^{-1}$ after 1000 cycles, equivalent to the low capacity decrement of 0.049% per cycle. In contrast, the batteries with cCoP@CNTs, KB, and PP only show 903, 627.9, and 450.6 mAh g$^{-1}$, respectively. The
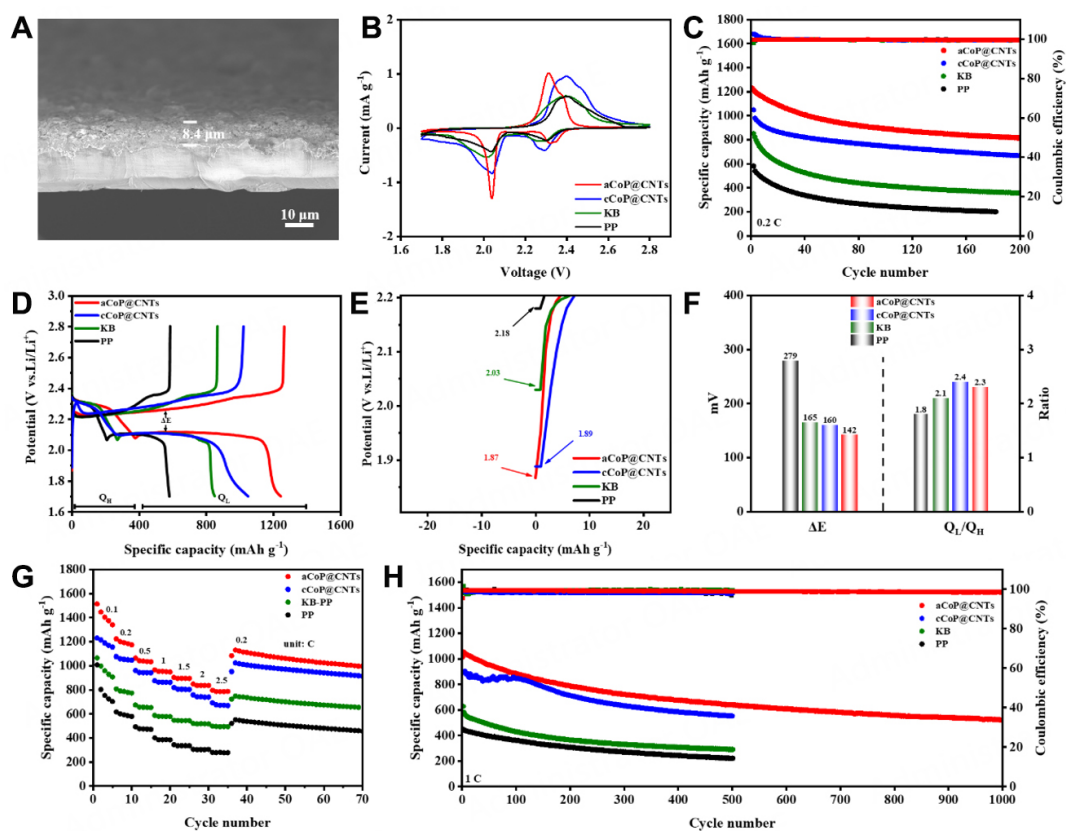
**Figure 4.** (A) Cross-sectional SEM image of the aCoP@CNTs modified separator; (B) CV curves of the cells with different separators under scan rate of 0.1 mV s$^{-1}$; (C) cycling performance of the Li-S cells with different separators at 0.2 C; (D) discharge/charge profiles of cells with different separators and the corresponding discharge initial potential (E); (F) the histogram of polarization potential and $Q_L/Q_H$ value derived from charge/discharge profiles; (G) the rate performance and long-term cycling stability at 1C (H) of the batteries with different separators.

satisfactory long-cycle performance could mainly be ascribed to the strong chemical bond between amorphous CoP particles and PSs, thus ensuring high sulfur utilization and low-capacity decay rate. In addition, Supplementary Figure 13 presents the Nyquist plots of Li-S batteries with various modification separators after cycling. There are two semicircles in the impedance spectrum of all batteries from the middle frequency regions to the high-frequency regions, which correspond to charge transfer resistance ($R_{ct}$) and interface resistance ($R_f$), respectively[59,60]. The fitting result of Nyquist plots shows that the sum of $R_f$ and $R_{ct}$ of the battery with aCoP@CNTs electrode (38.1 Ω) after cycling is lower than that of the cCoP@CNTs (44.0 Ω), KB (61.3 Ω) and PP (103.1 Ω). The result of EIS spectra matches well with the above consequence of Li$^+$ diffusion, further confirming that the battery with aCoP@CNTs separator possesses a higher electrocatalytic ability and effectively reduces electrochemical polarization, thus leading to the rapid transmission of electrons/ions.

Simple visual PSs permeation experiments were used to intuitively observe the excellent adsorption capacity of aCoP@CNTs functional electrocatalyst for PSs, as shown in Figure 5A. The inner small bottle contains Li$_2$S$_6$ solution, the outer large bottle contains solvent ($V_{DOL}$:$V_{DME}$ = 1:1), and the inner bottles were sealed with different separators. After standing for 24 h, the bottle with the pristine PP separator experienced serious color change and showed brownish yellow due to severe PSs penetration. For the outer bottle with aCoP@CNTs separator, only a few yellow polysulfides infiltrated into the outer bottle, confirming the
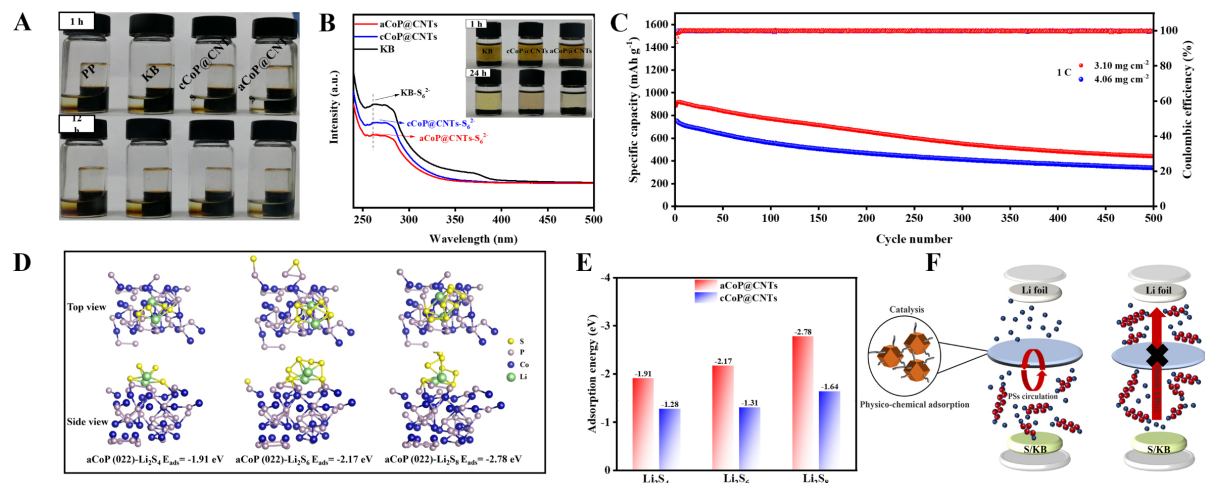
**Figure 5.** (A) The visualized adsorption test of $Li_2S_6$; (B) UV-vis spectra after adsorption for 24 h; (C)long-term cycling performance of the Li-S cells with aCoP@CNTs modified separator under high sulfur loading; (D) top and side view of PSs molecule on aCoP surfaces; (E) adsorption energy between $Li_2S_x$ (x = 2,4 and 6) and aCoP@CNTs and cCoP @CNTs surface; (F) schematic diagram of the Li-S batteries with (right) and without (left) aCoP@CNTs modified separator.

superior capacity of aCoP@CNTs for PSs. A facile visual adsorption test was used to further prove the excellent adsorption of aCoP@CNTs to PSs. Figure 5B presents that 1M brown $Li_2S_6$ electrolyte was added to KB, aCoP@CNTs, and cCoP@CNTs materials of the same mass. After standing for 24 h, compared with KB and cCoP@CNTs, it can be observed that the solution containing aCoP@CNTs turned nearly transparent. UV-vis spectroscopy was also applied to the supernatant after PSs adsorption and further investigated the adsorption capacity of various materials. After the adsorption reaction with different materials, the supernatant with aCoP@CNTs delivered a lower UV-vis absorbance than that containing other materials, revealing the strong interaction between amorphous CoP and PS.

The long cycle stability of Li-S cells under high sulfur loading was tested to evaluate the potential of the modified diaphragm in practical application, shown in Figure 5C. At the current density of 1 C, the batteries with aCoP@CNTs interlayer exhibit an excellent discharge specific capacity of 886 mAh $g^{-1}$ and 753.6 mAh $g^{-1}$ under high sulfur loading of 3.1 and 4.06 mg $cm^{-2}$, respectively. After 500 cycles, the batteries remain gratifying discharge capacity of 441.2 mAh $g^{-1}$ and 340.4 mAh $g^{-1}$ with high average coulombic efficiency of 99.7% and 99.6%, respectively.

Then, to further deepen the atomic-level insight into the adsorption behavior of crystalline and amorphous CoP for PSs. the adsorption properties of long-chain PSs ($Li_2S_x$, x = 4, 6 and 8) on the (022) planes of crystalline and amorphous CoP were studied by DFT calculations. The most stable adsorption configurations of top and side views for long-chain PSs on crystalline and amorphous CoP surface are displayed in Figure 5D and Supplementary Figure 14. The specific calculation results are shown in Figure 5E. The aCoP@CNTs s (-1.91 eV for $Li_2S_4$, -2.17 eV for $Li_2S_6$, and -2.78 eV for $Li_2S_8$) render adsorption energy of more negative value for long-chain PSs than cCoP@CNTs (-1.28 eV for $Li_2S_4$, -1.31 eV for $Li_2S_6$ and -1.64 eV for $Li_2S_8$). Overall, the above DFT and experiment results demonstrated a strong interaction between PSs and amorphous CoP. Therefore, as shown in Figure 5F, the outstanding performance could be attributed to the merits of the robust physico-chemical adsorption and electrocatalyst capacity of amorphous CoP. Specifically, the cross-linked stacked CNTs act as an excellent conductive network and provide rich ion/electronic transmission; additionally, CNTs can also serve as physical barriers

to restrict the shuttle effect. Furthermore, the amorphous CoP supported on CNTs network provides rich unsaturated dangling bonds and strong Co-S bond interaction for PSs, which promotes the conversion of PSs and further limits the shuttle effect.

## CONCLUSIONS

In summary, we have successfully fabricated aCoP@CNTs and cCoP@CNTs electrocatalysts as functional separators for high-stability Li-S batteries and demonstrated that the unsaturated Co in amorphous CoP could rapidly adsorb PSs and promote the conversion reaction of soluble PSs to solid $Li_2S$. Meanwhile, the *in-situ* introduction of CNTs could effectively improve the conductivity of the catalytic interface and remedy the low crystallinity of carbon after annealing at a lower temperature, ensuring the electrical conductivity, and enlarging the specific surface area of the separator. Therefore, the Li-S batteries with a functional aCoP@CNTs modified separator exhibit high initial discharge capacity, excellent rate performance, and good long-term stability under high sulfur loading. This work provides a novel perspective for the introduction of amorphous materials as the key components and highlights its unlimited possibilities for practical application in high-performance Li-S batteries.

## DECLARATIONS

### Authors' contributions
Conceived the study, designed the experiments and wrote the manuscript: Feng J, Song J
Carried out the synthesis and characterization: Feng J, Li J, Zhang H, Liu W, Lin Z, Wang T, Zhao X, Wang F
Gave advice to the research: Wang T, Sun B
Supervision, review and editing: Zhao X, Wang F, Song J
All authors discussed the results and commented on the manuscript.

### Availability of data and materials
More data on the results of our finding can be found in the Supplementary Material.

### Conflicts of interest
All authors declared that there are no conflicts of interest.

### Ethical approval and consent to participate
Not applicable.

### Consent for publication
Not applicable.

## REFERENCES

1.  Zhou G, Chen H, Cui Y. Formulating energy density for designing practical lithium-sulfur batteries. *Nat Energy* 2022;7:312-9.  DOI
2.  Hu Y, Chen W, Lei T, et al. Strategies toward high-loading lithium-sulfur battery. *Adv Energy Mater* 2020;10:2000082.  DOI
3.  Yang X, Li X, Adair K, et al. Structural design of lithium-sulfur batteries: from fundamental research to practical application. *Electrochem Energy Rev* 2018;1:239-93.  DOI
4.  Li G, Wang S, Zhang Y, et al. Revisiting the role of polysulfides in lithium-sulfur batteries. *Adv Mater* 2018;30:e1705590.  DOI  PubMed
5.  Song J, Guo X, Zhang J, et al. Rational design of free-standing 3D porous MXene/rGO hybrid aerogels as polysulfide reservoirs for high-energy lithium-sulfur batteries. *J Mater Chem A* 2019;7:6507-13.  DOI
6.  He J, Bhargav A, Manthiram A. Molybdenum boride as an efficient catalyst for polysulfide redox to enable high-energy-density lithium-sulfur batteries. *Adv Mater* 2020;32:e2004741.  DOI  PubMed
7.  Xie Y, Cao J, Wang X, Li W, et al. MOF-derived bifunctional $Co_{0.85}$Se nanoparticles embedded in n-doped carbon nanosheet arrays as efficient sulfur hosts for lithium-sulfur batteries. *Nano Lett* 2021;21:8579-86.  DOI
8.  Song C, Jin Q, Zhang W, et al. Prussian blue analogs derived Fe-Ni-P@nitrogen-doped carbon composites as sulfur host for high-performance lithium-sulfur batteries. *J Colloid Interf Sci* 2021;595:51-8.  DOI  PubMed
9.  Yu Y, Yan M, Dong W, et al. Optimizing inner voids in yolk-shell $TiO_2$ nanostructure for high-performance and ultralong-life lithium-sulfur batteries. *Chem Eng J* 2021;417:129241.  DOI
10.  Yu P, Feng L, Ma D, et al. Template-free self-caging nanochemistry for large-scale synthesis of sulfonated-graphene@sulfur nanocage for long-life lithium-sulfur batteries. *Adv Funct Mater* 2021;31:2008652.  DOI
11.  Song X, Wang S, Chen G, et al. Fe-N-doped carbon nanofiber and graphene modified separator for lithium-sulfur batteries. *Chem Eng J* 2018;333:564-71.  DOI
12.  Li C, Liu R, Xiao Y, et al. Recent progress of separators in lithium-sulfur batteries. *Energy Storage Mater* 2021;40:439-60.  DOI
13.  Feng J, Li Y, Yuan J, et al. Energy-saving synthesis of functional $CoS_2$/rGO interlayer with enhanced conversion kinetics for high-performance lithium-sulfur batteries. *Front Chem* 2022;9:830485.  DOI
14.  Li Q, Liu Y, Yang L, et al. N, O co-doped chlorella-based biomass carbon modified separator for lithium-sulfur battery with high capacity and long cycle performance. *J Colloid Interf Sci* 2021;585:43-50.  DOI  PubMed
15.  Shin H, Baek M, Gupta A, et al. Recent progress in high donor electrolytes for lithium-sulfur batteries. *Adv Energy Mater* 2020;10:2001456.  DOI
16.  Yang Q, Deng N, Chen J, et al. The recent research progress and prospect of gel polymer electrolytes in lithium-sulfur batteries. *Chem Eng J* 2021;413:127427.  DOI
17.  Zhou Z, Sun T, Cui J, et al. A homogenous solid polymer electrolyte prepared by facile spray drying method is used for room-temperature solid lithium metal batteries. *Nano Res* 2021.  DOI
18.  Tran M X, Enggar Anugrah Ardhi R, Liu G, et al. Plasma-polymerized $C_{60}$-coated CNT interlayer with physical and chemical functions for lithium-sulfur batteries. *Chem Eng J* 2020;401:126075.  DOI
19.  Zheng M, Chi Y, Hu Q, et al. Carbon nanotube-based materials for lithium-sulfur batteries. *J Mater Chem A* 2019;7:17204-41.  DOI
20.  Huo J, Shen Z, Cao X, et al. Macro/micro-environment regulating carbon-supported single-atom catalysts for hydrogen/oxygen conversion reactions. *Small* 2022;18:2202394.  DOI  PubMed
21.  Li J, Zhang H, Luo L, et al. Blocking polysulfides with a Janus $Fe_3C$/N-CNF@RGO electrode via physiochemical confinement and catalytic conversion for high-performance lithium-sulfur batteries. *J Mater Chem A* 2021;9:2205-13.  DOI
22.  Jing F, Ma Z, Wang J, et al. Oxygen vacancy inducing phase transition during charge storage in $MnO_x$@rGO supercapacitor electrode. *Chem Eng J* 2022;435:135103.  DOI
23.  Fan L, Wu H, Wu X, et al. Fe-MOF derived jujube pit like $Fe_3O_4$/C composite as sulfur host for lithium-sulfur battery. *Electrochim Acta* 2019;295:444-51.  DOI
24.  Cao X, Huo J, Li L, et al. Recent advances in engineered ru-based electrocatalysts for the hydrogen/oxygen conversion reactions. *Adv Energy Mater* 2022;12:2202119.  DOI
25.  Liu H, Liu X, Li W, et al. Porous carbon composites for next generation rechargeable lithium batteries. *Adv Energy Mater* 2017;7:1700283.  DOI
26.  Chung S, Manthiram A. High-performance Li-S batteries with an ultra-lightweight MWCNT-coated separator. *J Phys Chem Lett* 2014;5:1978-83.  DOI  PubMed
27.  Zhou G, Li L, Wang D, et al. A flexible sulfur-graphene-polypropylene separator integrated electrode for advanced Li-S batteries. *Adv Mater* 2015;27:641-7.  DOI  PubMed
28.  Chen Y, Wang T, Tian H, et al. Advances in lithium-sulfur batteries: from academic research to commercial viability. *Adv Mater* 2021;33:2003666.  DOI  PubMed
29.  Ma L, Yu L, Liu J, et al. Construction of $Ti_4O_7$/TiN/carbon microdisk sulfur host with strong polar N-Ti-O bond for ultralong life lithium-sulfur battery. *Energy Storage Mater* 2022;44:180-9.  DOI
30.  Lu K, Zhang H, Gao S, et al. Manipulating polysulfides conversion with strongly coupled $Fe_3O_4$ and nitrogen doped carbon for stable and high capacity lithium-sulfur batteries. *Adv Funct Mater* 2019;29:1807309.  DOI
31.  Li Q, Ma Z, Zhao J, et al. A flexible self-supporting ultralong $MnO_2$ nanowires-expanded graphite nanosheets current collector with

enhanced catalytic reaction kinetics for high-loading lithium-sulfur batteries. *J Power Sources* 2022;521:230929.  DOI

32.  Wang S, Hou X, Zhong Z, et al. $Co_3O_4$-NP embedded mesoporous carbon rod with enhanced electrocatalytic conversion in lithium-sulfur battery. *Sci Rep* 2018;8:16133.  DOI  PubMed  PMC

33.  Xu K, Liang X, Wang L, et al. Tri-functionalized polypropylene separator by $rGO/MoO_2$ composite for high-performance lithium-sulfur batteries. *Rare Metals* 2021;40:2810-8.  DOI

34.  Xia G, Ye J, Zheng Z, et al. Catalytic FeP decorated carbon black as a multifunctional conducting additive for high-performance lithium-sulfur batteries. *Carbon* 2021;172:96-105.  DOI

35.  Zhang H, Xin S, Li J, et al. Synergistic regulation of polysulfides immobilization and conversion by MOF-derived CoP-HNC nanocages for high-performance lithium-sulfur batteries. *Nano Energy* 2021;85:106011.  DOI

36.  Zhang M, Guo Y, Wei Y, et al. Integrating conductivity and active sites: $Fe/Fe_3C@GNC$ as an trapping-catalyst interlayer and dendrite-free lithium host for the lithium-sulfur cell with outstanding rate performance. *J Mater Chem A* 2020;8:8987-19000.  DOI

37.  Zhou H, Sui Z, Amin K, et al. Investigating the electrocatalysis of a $Ti_3C_2$/carbon hybrid in polysulfide conversion of lithium-sulfur batteries. *ACS Appl Mater Interfaces* 2020;12:13904-13.  DOI

38.  Sun W, Li Y, Liu S, et al. Mechanism investigation of iron selenide as polysulfide mediator for long-life lithium-sulfur batteries. *Chem Eng J* 2021;416:129166.  DOI

39.  Li X, Su J, Li Z, et al. Revealing interfacial space charge storage of $Li^+/Na^+/K^+$ by operando magnetometry. *Sci Bull* 2022;67:1145-53.  DOI

40.  Liu S, Li Y, Zhang C, et al. Amorphous $TiO_2$ nanofilm interface coating on mesoporous carbon as efficient sulfur host for Lithium-Sulfur batteries. *Electrochim Acta* 2020;332:135458.  DOI

41.  Li R, Rao D, Zhou J, et al. Amorphization-induced surface electronic states modulation of cobaltous oxide nanosheets for lithium-sulfur batteries. *Nature Commun* 2021;12:3102.  DOI  PubMed  PMC

42.  Chen X, Ding X, Wang C, et al. A multi-shelled CoP nanosphere modified separator for highly efficient Li-S batteries. *Nanoscale* 2018;10:13694-701.  DOI  PubMed

43.  Li C, Xi Z, Guo D, et al. Chemical immobilization effect on lithium polysulfides for lithium-sulfur batteries. *Small* 2018;14:1701986.  DOI  PubMed

44.  Jin R, Zhai Q, Wang Q, et al. Amorphous transition metal sulfides anchored on amorphous carbon-coated multiwalled carbon nanotubes for enhanced lithium-ion storage. *Chem Eur J* 2017;23:14056-63.  DOI  PubMed

45.  Liu L, Li Y, Zhang Y, et al. CoP@C with chemisorption-catalysis effect toward lithium polysulfides as multifunctional interlayer for high-performance lithium-sulfur batteries. *Electrochim Acta* 2022;419:140391.  DOI

46.  Qin B, Cai Y, Wang P, et al. Crystalline molybdenum carbide-amorphous molybdenum oxide heterostructures: in situ surface reconfiguration and electronic states modulation for Li-S batteries. *Energy Storage Mater* 2022;47:345-53.  DOI

47.  Ye Z, Jiang Y, Qian J, et al. Exceptional adsorption and catalysis effects of hollow polyhedra/carbon nanotube confined CoP nanoparticles superstructures for enhanced lithium-sulfur batteries. *Nano Energy* 2019;64:103965.  DOI

48.  Zhang D, Luo Y, Wu B, et al. A heterogeneous FeP-CoP electrocatalyst for expediting sulfur redox in high-specific-energy lithium-sulfur batteries. *Electrochim Acta* 2021;397:139275.  DOI

49.  Xu Y, Mo Y, Tian J, et al. The synergistic effect of graphitic N and pyrrolic N for the enhanced photocatalytic performance of nitrogen-doped graphene/$TiO_2$ nanocomposites. *Appl Catal B Environ* 2016;181:810-7.  DOI

50.  Nita C, Fullenwarth J, Monconduit L, et al. Eco-friendly synthesis of $SiO_2$ nanoparticles confined in hard carbon: a promising material with unexpected mechanism for Li-ion batteries. *Carbon* 2019;143:598-609.  DOI

51.  Zhou W, Zhao D, Wu Q, et al. Amorphous CoP nanoparticle composites with nitrogen-doped hollow carbon nanospheres for synergetic anchoring and catalytic conversion of polysulfides in Li-S batteries. *J Colloid Interf Sci* 2021;603:1-10.  DOI  PubMed

52.  Sun R, Bai Y, Luo M, et al. A enhancing polysulfide confinement and electrochemical kinetics by amorphous cobalt phosphide for highly efficient lithium-sulfur batteries. *ACS Nano* 2021;15:739-50.  DOI  PubMed

53.  Zhou Q, Yang X, Xiong X, et al. A solid electrolyte based on electrochemical active $Li_4Ti_5O_{12}$ with PVDF for solid state lithium metal battery. *Adv Energy Mater* 2022;12:2201991.  DOI

54.  He J, Bhargav A, Manthiram A. Covalent organic framework as an efficient protection layer for a stable lithium-metal anode. *Angew Chem Int Ed* 2022;61:e202116586.  DOI  PubMed

55.  Zhu Q, Xu H, Shen K, et al. Efficient polysulfides conversion on $Mo_2CT_x$ MXene for high-performance lithium-sulfur batteries. *Rare Metals* 2021;41:311-8.  DOI

56.  Li J, Song J, Luo L, et al. Synergy of MXene with Se infiltrated porous N-doped carbon nanofibers as janus electrodes for high-performance sodium/lithium-selenium batteries. *Adv Energy Mater* 2022;12:2200894.  DOI

57.  Ruan J, Sun H, Song Y, et al. Constructing 1D/2D interwoven carbonous matrix to enable high-efficiency sulfur immobilization in Li-S battery. *Energy Mater* 2021;1:100018.  DOI

58.  Castillo J, Qiao L, Santiago A, et al. Perspective of polymer-based solid-state Li-S batteries. *Energy Mater* 2022;2:200003.  DOI

59.  Cai M, Zhang H, Zhang Y, et al. Boosting the potassium-ion storage performance enabled by engineering of hierarchical MoSSe nanosheets modified with carbon on porous carbon sphere. *Sci Bull* 2022;67:933-45.  DOI

60.  Xiong X, Yan W, Zhu Y, et al. $Li_4Ti_5O_{12}$ Coating on copper foil as ion redistributor layer for stable lithium metal anode. *Adv Energy Mater* 2022;12:2103112.  DOI